Influence of the A-site cation on hysteresis and ion migration in lead-free perovskite single crystals

Naveen Kumar Tailor [1], Apurba Mahapatra,[2] Abul Kalam,[3] Manoj Pandey,[4] Pankaj Yadav [5,*] and Soumitra Satapathi [1,†]

[1]*Department of Physics, Indian Institute of Technology Roorkee, Haridwar, Uttarakhand 247667, India*
[2]*Department of Physics and Astronomy, National Institute of Technology, Rourkela 769008, India*
[3]*Department of Chemistry, Faculty of Science, King Khalid University, Abha 61413, P.O. Box 9004, Saudi Arabia*
[4]*Department of Chemistry, School of Technology, Pandit Deendayal Energy University, Gandhinagar-382007 Gujarat, India*
[5]*Department of Solar Energy, School of Technology, Pandit Deendayal Energy University, Gandhinagar-382 007 Gujarat, India*

Lead-free halide perovskites have recently emerged as promising photoactive materials due to their nontoxicity, stability, and unique photophysical properties. However, similar to lead-based perovskites, ion migration plays a significant role in determining their device potential and needs an in-depth understanding. Here, we study the role of A-site cation size and its nature on the ion transport dynamics in the $A_3Bi_2I_9$ [A= methylamine (MA) and formamidinium (FA)] perovskite single crystals (SCs) using the temperature-dependent electrochemical impedance spectroscopy. The activation energy was estimated as 0.54 and 0.66 eV with a corresponding trap density of 13×10^9 and $6.7 \times 10^9\,cm^{-3}$ for $MA_3Bi_2I_9$ and $FA_3Bi_2I_9$SC, respectively. The higher activation energy in $FA_3Bi_2I_9$SCs indicates suppressed ion migration which can be attributed to its large cation size leading to lattice enlargement and reduced rotational motion. Additionally, the less acidic and less polar character of the FA cation and strong hydrogen bond plays an important role to reduce the defect states. Furthermore, current-voltage (*I-V*) measurements also confirm the lower degree of hysteresis in $FA_3Bi_2I_9$SC than that of $MA_3Bi_2I_9$ SC, demonstrating lower ionic conductivity in these materials. Our paper provides a fundamental understanding of the role of the A-cation effect on the ionic and electrical responses in these lead-free SCs, which will be beneficial for designing the perovskite devices to improving their performance and overall stability.

I. INTRODUCTION

Lead halide perovskites (LHPs) have recently emerged as promising semiconducting material due to their excellent photophysical properties for developing highly efficient solar cells [1–5], light-emitting diodes [6], lasers [7], field-effect transistors [8,9], and photodetectors [10]. However, the toxicity of lead (Pb) poses serious environmental and health hazards and requires the replacement of lead with a relatively less toxic isoelectronic element without compromising much of its performance [11]. This has fueled up the development of several lead-free halide perovskites with different metal cations, namely, Bi, Sn, Sb, Ge, etc. for optoelectronics applications [12–16]. However, photostability and light-induced degradation are some of the challenges that need to be catered to for future advances [17,18]. Notably, the ion transport dynamics which is probably the main reason for the occurrence of hysteresis in *I-V* characteristics, the slow conductivity response, and the large dielectric constant remain elusive [19–21]. To date, significant efforts have been devoted to understanding ion migration in LHPs and several strategies are proposed for the reduction of ion migration [19,20,22–26]. Unfortunately, the understanding and cause of hysteresis and ion migration in lead-free perovskite SCs are still ambiguous, and only a few studies are reported. In this context, it is critical to comprehend the ion dynamics of these materials in order to improve the performance of the devices fabricated using these materials.

Out of several lead-free perovskites, isoelectronic Bi (Bi^{3+} have $6s^2$ lone pair same as Pb^{2+}) based lead-free perovskites with the $A_3Bi_2I_9$ [A = methylammonium (MA), formamidinium (FA), Cs, Rb, etc.] crystal structure are particularly interesting due to their nontoxicity and rich structural diversity [12,16,27]. These $A_3Bi_2I_9$ perovskites adopt an ordered vacancy structure and demonstrate greater thermal and phase stability compared with lead-based halide perovskites. Apart from being used in solar cell devices, these Bi halides have attracted much attention as high-energy radiation detectors and imaging devices for medical diagnostics [12,28]. Consequently, in recent years, extensive efforts have been devoted to understanding their optical and electric properties. However, to optimize the device potential of these Bi-based lead-free perovskite materials, an in-depth understanding of carrier transport especially ion dynamics, ionic conductivity, *I-V* hysteresis, and their impact on stability and device performance need to be studied in detail.

Several experimental and theoretical approaches have been reported in the literature to quantify ion dynamics of perovskite film including temperature-dependent impedance spectroscopy [29], photothermal induced resonance microscopy [30], photoinduced current transient spectroscopy [31], muon spin relaxation [32], transient capacitance measurements [33], Kelvin probe force microscopy [22,34,35], and first-principles DFT calculation [20,26]. All of these stud-

*Corresponding author: Pankaj.Yadav@sse.pdpu.ac.in
†soumitrasatapathi@gmail.com

ies reveal that both anions and cations can migrate due to the presence of vacancies, interstitials, or antisite substitutions [19,24,36]. However, based on different experimental techniques, a large variation in the activation energies for ion migration has been reported. Furthermore, the A-site cation engineering significantly alters the properties of the perovskite crystal structure [29]. The A-site cation is an essential part of the perovskite lattice, and its orientations, size, and nature are likely coupled to the material structure and dynamics [27,37,38]. Various investigations have recommended that A cations play a significant role to determine the optoelectronic performance of perovskite devices [39–44]. However, there is still a lack of comprehensive understanding of the *A*-site cation effect on ionic migration and *I-V* hysteresis. An in-depth understanding of ionic migration and *A*-site cationic effect on the activation energy and ionic conductivity is required for optimizing the performance of lead-free perovskite SC-based devices.

Here, we have investigated the effect of A-cation size and nature on the ionic and electrical transport properties of as-grown $MA_3Bi_2I_9$ and $FA_3Bi_2I_9$ perovskite SCs. Interestingly, we observe that introducing the larger A cation leads to the larger unit cell and lower band gap. We have calculated the ionic and electronic transport parameters and find that $FA_3Bi_2I_9$SC exhibit higher activation energy and lower trap states. Additionally, the *I-V* curve was measured with temperature variation to investigate the degree of hysteresis in both SCs. As expected, $FA_3Bi_2I_9$SCs show a lower degree of *I-V* hysteresis due to higher ion conduction activation energy. In addition, we have provided outlook that needs to be addressed in the future to understand the ionic and electronic transport in these materials.

II. METHODS

A. Materials and crystal growth

Methylammonium iodide (MAI) (>99.0%), formamidinium iodide (FAI) (>99.0%), and bismuth iodide anhydrous (BiI_3) (>98.0%) was purchased from the TCI chemicals. GBL (γ-butyrolactone) extra pure was purchased from SRL. All chemicals were used as received without further purification. Growth of the $MA_3Bi_2I_9$ and $FA_3Bi_2I_9$ single crystals was carried out by inverse temperature crystallization (ITC) method. According to the stoichiometric ratio of $A_3Bi_2I_9$, ($A = MA$ and FA) 3-mol AI and 2-mol BiI_3 were dissolved into 1.2-ml GBL under continuous magnetic stirring at 60 °C until no powder is observed. Now the temperature was increased up to 120 °C with a heating rate of 0.5 °C per hour. At 120 °C we put the solution for 2 days. After 2 days, we obtained millimeter-sized SCs. There was no seed placed in solution so homogeneous nucleation occurs and single crystals grew in this process.

B. Characterizations

Photographs of crystals were taken using a DSLR camera. Powder x-ray-diffraction pattern was measured using a Bruker (D8-Advance model) diffractometer equipped with a LINXEYE XE detector under Cu $K\alpha$ radiation ($\lambda = 1.54$ Å). The absorbance spectra of crystals was measured using Microprocessor UV-visible double beam spectrophotometer LI-2800. For the Raman spectra measurement, the WITec α300 RA Raman instrument was used with the laser source 532 nm. Electrochemical impedance spectroscopy (EIS) measurements were performed using a potentiostat autolab equipped with a frequency response analyzer. EIS measurements were performed as a function of temperature.

III. RESULTS AND DISCUSSION

A. Structural analysis

The lead-free $A_3Bi_2I_9$SCs with two different sized organic cations $A = MA^+$ (2.17 Å) and FA^+ (2.53 Å) were grown using the solution-processed ITC technique. The images of as-grown crystals are presented in Fig. S1 of the Supplemental Material [45]. The crystal structure of $MA_3Bi_2I_9$ and $FA_3Bi_2I_9$ is presented in Figs. 1(a) and 1(b), respectively. Both crystals possess a zero-dimensional structure. In $MA_3Bi_2I_9$, the face-shared BiI_6 bioctahedra or $(Bi_2I_9)^{3-}$ clusters are separated by $CH_3NH_3^+$ groups. Similarly, in $FA_3Bi_2I_9$, the FA^+ ions are distributed around the isolated $(Bi_2I_9)^{3-}$ dioctahedral. In these structures, a hydrogen bond (H bond) forms between the H^+ ion and the I^- ions which leads to stretching in $(Bi_2I_9)^{3-}$, enhances the Bi-Bi distance and the band gap. The hydrogen-bonding interaction is larger for the FA^+ cation because of two NH_2 groups. Additionally, MA^+ is a sp^3-hybridized polar cation whereas FA^+ is a sp^2 polar cation. The positive charge in MA^+ is mainly localized toward its $-NH_3$ moiety and in FA^+, it is delocalized between the two $-NH_2$ groups. The FA^+ cation has a significantly smaller dipole moment than the MA^+ cation [46].

The crystalline quality of as-grown SCs was investigated using the x-ray diffraction (XRD) technique. The XRD pattern of $MA_3Bi_2I_9$ and $FA_3Bi_2I_9$SCs [Fig. 1(c)] reveals that the (006) peaks show the highest intensity which can be assigned to the preferential orientation along the *c* axis. The crystal structure of both crystals belongs to the hexagonal system with the $P6_3mmc$ space group [27]. The corresponding lattice parameters of these SCs are estimated as $a = 8.58$, $b = 8.58$, and $c = 21.74$ Å for $MA_3Bi_2I_9$ SC and $a = 8.77$, $b = 8.77$, and $c = 22.11$ Å for $FA_3Bi_2I_9$SC. The larger cation requires a longer distance between the crystal lattice planes and, hence, lattice parameters enhance in $FA_3Bi_2I_9$. The enhancement of the lattice unit cell because of the large A-site cation can be attributed to elongatement of Bi_2I_9 bioctahedra due to long-range hydrogen bonding. The XRD patterns of crystals exhibit prominent peaks at 8.23°, 16.26°, and 24.54° for $MA_3Bi_2I_9$ SC and $2\theta = 8.10°$, 16.04°, and 24.08° for $FA_3Bi_2I_9$SC. We observed that major peaks in the $FA_3Bi_2I_9$ crystal; gradually shift to lower 2θ values in comparison to the $MA_3Bi_2I_9$ crystal. Additionally, for confirming the phase purity of grown SCs, we performed the precursors XRD and presented them in Fig. S2 of the Supplemental Material [45]. We did not find any crystalline residue from either FAI or BiI_3 in the $FA_3Bi_2I_9$SC, MAI, and BiI_3 in the $MA_3Bi_2I_9$ SC.

B. Optical properties

Furthermore, we performed steady-state diffuse reflectance spectroscopy to investigate the absorption profile and band
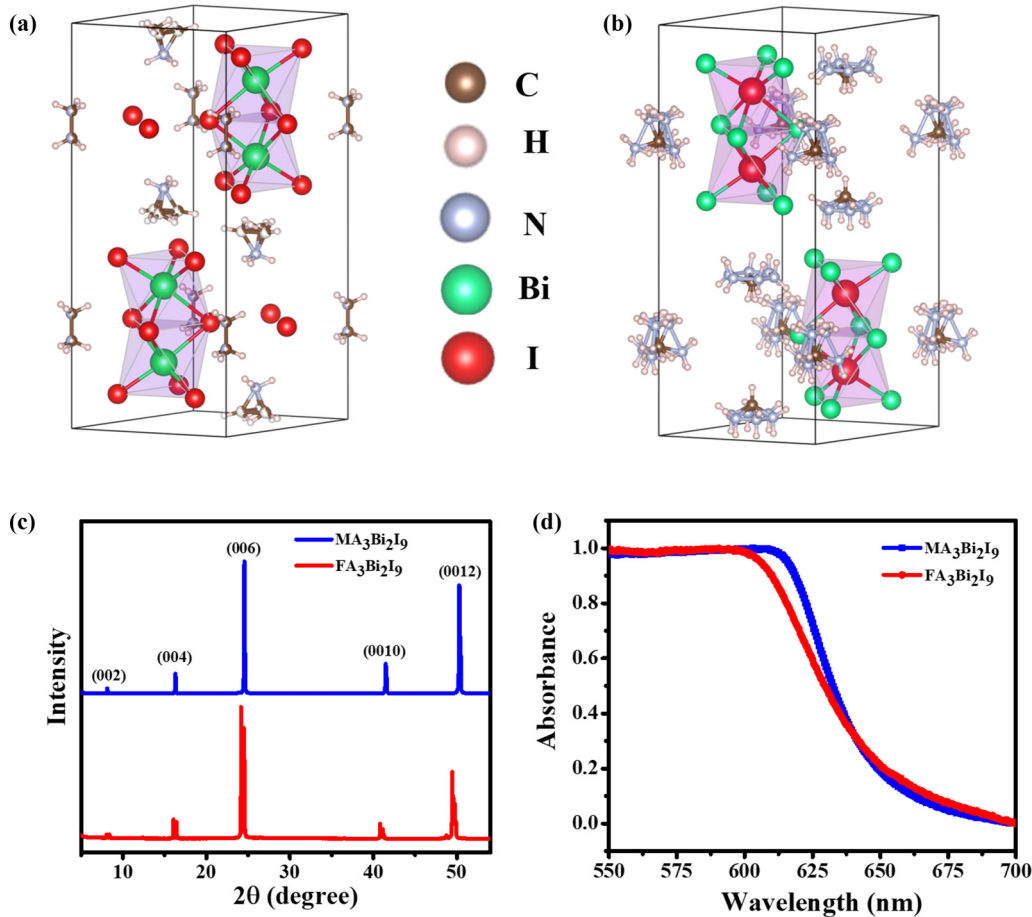
FIG. 1. Crystal structure of (a) $MA_3Bi_2I_9$ and (b) $FA_3Bi_2I_9$. [MA= CH_3NH_3, FA = $CH(NH_2)_2$] (c) XRD pattern and (d) the calculated absorption spectra from diffuse reflection spectra for $MA_3Bi_2I_9$ SC and $FA_3Bi_2I_9$SC.

gap. We calculated the absorption spectra as presented in Fig. 1(d). The absorbance spectra for both crystals indicate the clear band-edge cutoffs with negligible excitonic signature. The indirect band gap was calculated using the Tauc plot and values are estimated as $E_g = 1.75$ eV for $FA_3Bi_2I_9$ and $E_g = 1.81$ eV for $MA_3Bi_2I_9$ SC (Fig. S3 of the Supplemental Material) [45]. The cation size has a significant impact on the absorption region, and it is well documented in the case of lead halide perovskite SCs [47]. Usually, the large-radii A cations result in the lower band gap in lead halide perovskites. In our case of Bi-halide SCs, we observe that the introduction of the larger A cation extends the absorption edge and reduces the band gap. Although the A cation does not participate in the bands formation, the interaction of the A cation with the inorganic framework can affect the optical properties. The band gap in these structures arises because of the hybridization of Bi $6s$, $6p$, and I $5p$ states. The A cation can affect the band gap by the chemical pressure because of the cation size and the strength of H bonds [48]. As we discussed above that H-bond strength is larger in $FA_3Bi_2I_9$, which can reduce the band gap. The large-sized FA cation induces the chemical pressure to compress the Bi_2I_9 bioctahedra, enhances the overlap between Bi $6s/6p$ and I $5p$ states, which results in the reduction of the band gap. However, in these lead-free crystals, the A-site cation size effect is weaker than reported lead halide SCs which is due to the less connectivity of A cations with the

$[Bi_2I_9]^{3-}$ octahedra [49]. To investigate the structural features and the role of Bi-*X* bonds, we measured the Raman spectra of both crystals. In these crystals, the dominant vibrations occur due to strongly bound $[Bi_2I_9]^{3-}$ unit with the bridging MA^+ and FA^+ cations. We observed that the Raman peaks occur at 84, 110, 132, and 143 cm^{-1} in the $MA_3Bi_2I_9$ SC and 85, 111, and 145 cm^{-1} in the $FA_3Bi_2I_9$SC (Fig. S4 of the Supplemental Material) [45]. The peak at 110 and 84 cm^{-1} in $MA_3Bi_2I_9$ and 111 and 85 cm^{-1} in $FA_3Bi_2I_9$ are assigned to the bridging Bi-I symmetric and asymmetric stretching vibrations, respectively. The peak at 143 and 132 cm^{-1} in $MA_3Bi_2I_9$ and 145 cm^{-1} in $FA_3Bi_2I_9$ are assigned to the symmetric and asymmetric terminal Bi-I stretchs, respectively. However, we do not observe Raman modes at the low-frequency regime probably due to the less ionic interaction between MA^+ and FA^+ cations and $[Bi_2I_9]^{3-}$.

C. Electrical and ionic properties

The role of the A cation on the electrical properties of Bi-halide perovskite SCs was studied by using EIS and current-voltage (*J-V*) measurements as a function of temperature. In EIS measurements frequency in the range of 1 MHz to 1 Hz and the AC perturbation signal of 25 mV is used. The Nyquist spectra of both the SCs are measured under dark as a function of temperature and are shown in Figs. 2(a) and 2(b).
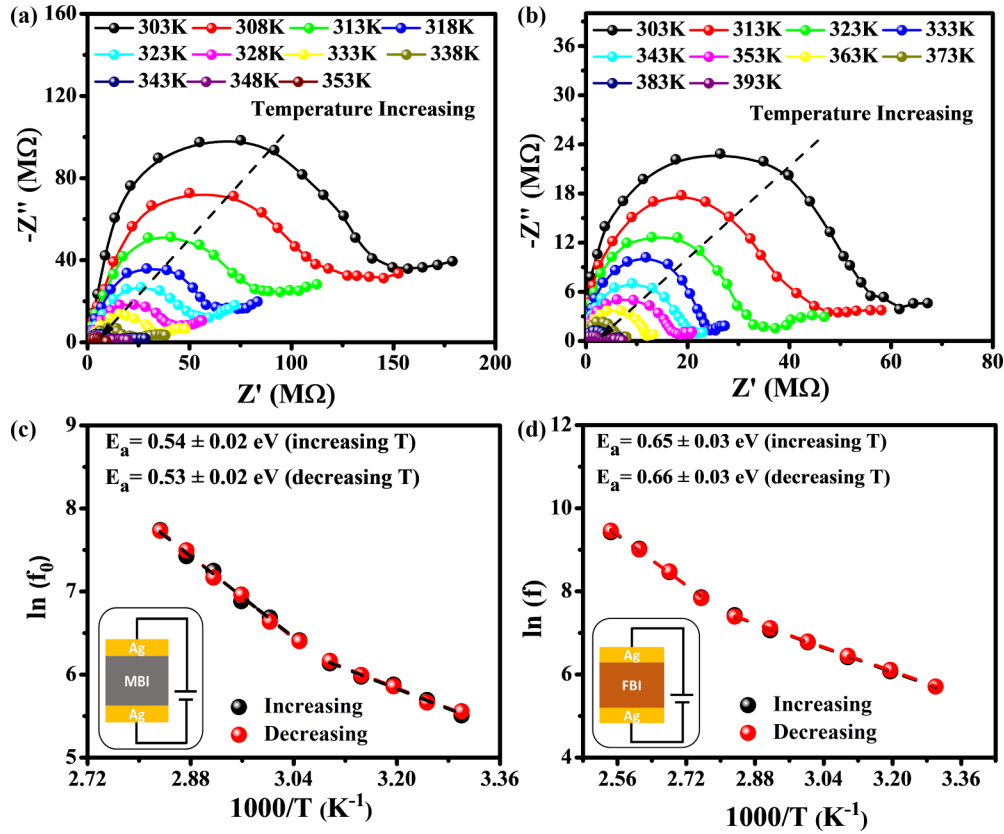
FIG. 2. Dark EIS measurement at 0-V DC bias in the frequency range of 1 MHz to 1 Hz as a function of temperature for (a) $MA_3Bi_2I_9$ and (b) $FA_3Bi_2I_9$SC. Arrhenius plots of the inflection frequencies vs $1000/T$ [$\ln(f_0)$ vs $1000/T$] during increasing and decreasing the temperature of the for (c) $MA_3Bi_2I_9$ and (d) $FA_3Bi_2I_9$SC. The value of E_a shows the activation energy for ion migration.

The obtained Nyquist spectra of SCs exhibit similar behavior during increase and decrease temperature cycles, which confirmed the thermal stability of SCs in the temperature, range (303–353 K for $MA_3Bi_2I_9$ and 303–393 K for $FA_3Bi_2I_9$). We observed better thermal stability in $FA_3Bi_2I_9$SCs than $MA_3Bi_2I_9$ SCs (Fig. S5 of the Supplemental Material) [45]. It is found that the thermal stability of the perovskite material directly relates to the acidity of the organic cation [50]. Due to the acidic character, the organic cation can be deprotonated to yield hydroiodic acid (HI). The FA cation has a less acidic character in comparison to the MA cation, which results in higher thermal stability of $FA_3Bi_2I_9$SC [51]. FA^+ also has a higher propensity to form hydrogen bonds. Therefore, the stronger H bond forms between FA^+ and I^- in $FA_3Bi_2I_9$ because of the enhanced number of protons in FA^+ than in MA^+. Furthermore, the strong H bond in $FA_3Bi_2I_9$ enhances the internal energy of this perovskite phase which helps to stabilize the structure and possess higher thermal stability.

As evident from Figs. 2(a) and 2(b), the diameter of the semicircles in both Nyquist plots reduce with the increase in temperature which indicates that the conductivity enhances and the associated resistances decrease. Additionally, the peak frequencies gradually shift to higher values with the increase in temperature which indicates that the relaxation time constant reduces with the temperature enhancement. Additionally, if we compare the Nyquist spectra of the $MA_3Bi_2I_9$ and $FA_3Bi_2I_9$ crystals at room temperature, we observed that the real value of the impedance in the $FA_3Bi_2I_9$ crystal is

smaller than that of the $MA_3Bi_2I_9$ crystal as is the radius in Nyquist spectra. This can be attributed to the better charge transport and lesser traps in $FA_3Bi_2I_9$ crystal [supported by the space-charge-limited current (SCLC) measurement, discussed in Fig. 4]. Next, we calculated the activation energies (E_a) from the Arrhenius plots of the try to escape frequencies (f_0) vs $1000/T$ [$n(f_0)$ vs $1000/T$] for both the SCs. The try to escape frequencies (f_0) calculate from the plots of the complex part of impedance as functions of frequency and temperature (Fig. S6 in the Supplemental Material) [45]. The activation energy of 0.26 and 0.54 eV are found for $MA_3Bi_2I_9$ SCs at the low- and high-temperature regions, respectively [Fig. 2(c)] [52,53]. In the case of $FA_3Bi_2I_9$SCs, the activation energy of 0.31 and 0.65 eV are obtained from the low- and high-temperature regions, respectively [Fig. 2(d)]. Previous studies suggest that the conductivity in perovskite SCs dominates by ionic conductivity at higher temperatures [28,29]. The ion conduction activation energy in $FA_3Bi_2I_9$ is 0.63 eV, which is greater than that of $MA_3Bi_2I_9$ SCs. The higher E_a and ion conductivity transition temperature in $FA_3Bi_2I_9$SCs suggests that ion migration in $FA_3Bi_2I_9$ is lower than $MA_3Bi_2I_9$ SCs. The variation in the ion conductivity transition temperature and E_a with cation size and nature can be attributed to the interaction between the ion and the perovskite lattice. It is also expected that the rotational dynamics of both the MA and the FA cations can alter the ion transport in these crystals. The MA cation assists the ion migration by reorienting its charge distribution along with the ionic motion, providing a
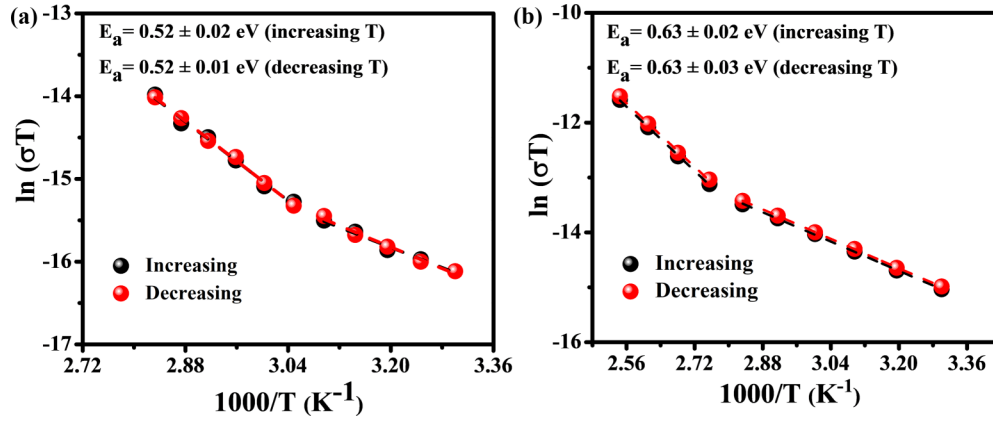
FIG. 3. Temperature-dependent conductivity Arrhenius plot of (a) $MA_3Bi_2I_9$ and (b) $FA_3Bi_2I_9$SCs.

local charge screening mechanism that boosts up the ionic migration [54]. Although the FA cation has less polar and less acidic character, and it is a less orientationally mobile cation. This characteristic of FA reduces the ion migration in $FA_3Bi_2I_9$SC. Previous studies by Li *et al.* showed that $FA_3Bi_2I_9$SC can endure the applied bias voltage up to 555 V which is almost five times higher than the $MA_3Bi_2I_9$ SC [28]. The higher ion activation energy in $FA_3Bi_2I_9$SC also ensures a comparably low dark current density and less noise under high external bias. Moreover, a larger value of E_a is also beneficial for the operational stability of the devices.

To further validate the activation energy results from EIS, we measured the temperature-dependent dark conductivity for both SCs and plotted in the Nerst-Einstein formalism Figs. 3(a) and 3(b)]. The activation energies are derived using the Nerst-Einstein expression,

$$\sigma T = \sigma_0 \left(-\frac{E_a}{k_B T} \right), \tag{1}$$

where k_B is the Boltzmann constant, T is the absolute temperature, and σ_0 is a constant [55]. The calculated activation energy of ions for both crystals is summarized in Table I. The obtained activation energies are in good agreement with our EIS findings and other reported values.

The charge-carrier transport parameters, defect densities, and hysteresis in current-voltage curves are important factors for the performance optimization of optoelectronic devices. To investigate the role of cations on defect densities and charge-carrier transport parameters on the bulk of SCs, we measured dark I-V with the increasing temperature [Figs. 4(a)

and 4(b)]. A change in slope changes with applied bias was observed for both SCs. Three distinct regions are marked in Figs. 4(a) and 4(b). It was observed that when the applied bias voltage (V) is lower than the kink-point voltage, the current enhances linearly V ($I \propto V$), which demonstrates an ohmic response between the electrode and the perovskite SCs. As V surpasses the kink-point voltage, I shows a fast nonlinear enhancement ($I \propto V^{n>3}$) indicating the trap states are filled by the injected charge carriers. The applied voltage at the kink point is defined as the trap-filled limit voltage (V_{TFL}) [57–59]. We used the SCLC method to calculate the charge trap density (η_{trap}) for both crystals.

The defect densities are computed using the given expression,

$$\eta_{trap} = \frac{2\varepsilon\varepsilon_0 V_{TFL}}{eL^2}, \tag{2}$$

where ε is termed as dielectric constant and L is termed as the thickness of the crystals. ε_0 is the vacuum permittivity, and e is the elementary charge (1.6×10^{-19} C), respectively [60]. The dielectric constants for $MA_3Bi_2I_9$ and $FA_3Bi_2I_9$SCs are 65 and 121, respectively [61]. The $FA_3Bi_2I_9$SCs show a lower trap density of 6.7×10^9 than 13×10^9 cm^{-3} for $MA_3Bi_2I_9$ SCs. These observations suggest that the large size of the FA cation and its less polar and acidic nature reduce the electronic traps inside the $FA_3Bi_2I_9$ perovskite lattice. The lower trap density in $FA_3Bi_2I_9$SC will be beneficial for charge collection and reduce carrier trapping and recombination.

The variation of conductivity as a function of temperature for both the crystals is shown in Fig. S7 of the Supplemental Material [45]. The conductivity of both the SCs

TABLE I. Calculated values of activation energy from the temperature-dependent IS and conductivity measurement.

Single crystals	Activation energy (Ev)		Measurements	References
	Low temperature	High temperature		
$MA_3Bi_2I_9$	0.26 ($T < 323$ K)	0.54 ($T > 323$ K)	Temperature-dependent EIS	This paper
$MA_3Bi_2I_9$	0.25 ($T < 323$ K)	0.52 ($T > 323$ K)	Temperature-dependent conductivity	
$MA_3Bi_2I_9$	*	0.46		[56]
$FA_3Bi_2I_9$	0.31 ($T < 353$ K)	0.66 ($T > 353$ K)	Temperature-dependent EIS	this paper
$FA_3Bi_2I_9$	0.29 ($T < 353$ K)	0.63 ($T > 353$ K)	Temperature-dependent conductivity	
$FA_3Bi_2I_9$	*	0.56		[28]
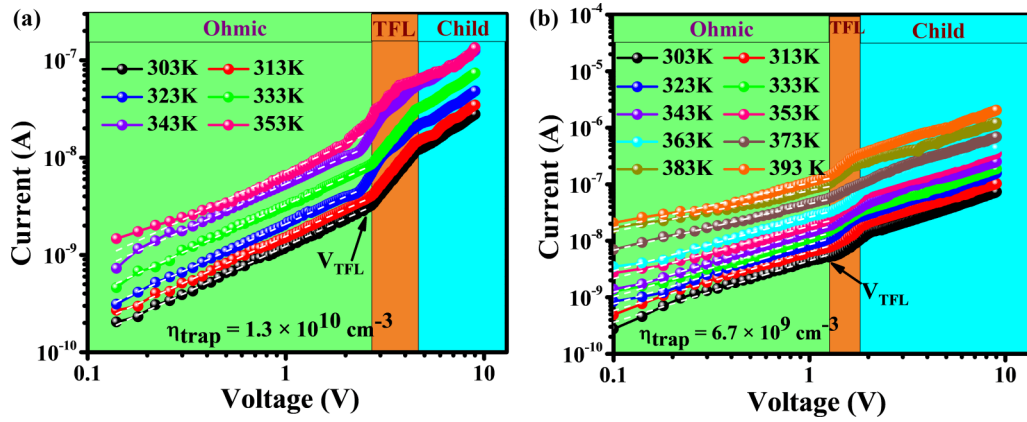
FIG. 4. Temperature-dependent *I-V* characteristics for (a) $MA_3Bi_2I_9$ and (b) $FA_3Bi_2I_9$SC.

exponentially increases with temperature. The higher ion conductivity transition temperatures of $FA_3Bi_2I_9$SCs suggest good thermal stability than the $MA_3Bi_2I_9$ crystal. The dark conductivity of $FA_3Bi_2I_9$SCs higher than the $MA_3Bi_2I_9$ SCs due to the lower electronic traps inside $FA_3Bi_2I_9$SCs. The dark current density at room temperature (303 K) for both crystals is shown in Fig. S8 of the Supplemental Material [45]. Both single crystals exhibited similar low dark current densities of about 10^{-11} A cm^{-2}. However, the $FA_3Bi_2I_9$SCs show reduced dark current density, which indicates low dark carrier concentration than the $MA_3Bi_2I_9$ SCs. The low dark carrier concentration, lower trap density, and higher dark conductivity $FA_3Bi_2I_9$SCs is in favor of making a better performance optoelectronics device than the $MA_3Bi_2I_9$ SCs.

The evolution of current-voltage hysteresis on temperature can be explained by the ion migration and charge trapping inside the SCs. Therefore, the *I-V* hysteresis was measured at different temperatures [Figs. 5(a) and 5(b)]. We find that the ion migration is temperature activated, and it enhances with increasing temperature. As a result, the *I-V* hysteresis for both crystals decreased with an increase in temperature. Figure 5(c) shows the *I-V* hysteresis for both crystals measured at a scan rate of 100 mV/s. As expected, $FA_3Bi_2I_9$SCs show a lower degree of *I-V* hysteresis due to higher ion conduction activation energy for $FA_3Bi_2I_9$SCs than $MA_3Bi_2I_9$ SCs. The defect or ion migration causes hysteresis in these crystals. The dynamics of the organic cations and those re-

lated to ion/defect migration are essentially coupled. The MA cation provides the local screening which boosts the ionic migration. The hysteresis measurements and conductivity studies show that FA cation improves the better electrical properties against temperature.

In this paper, we provided the influence of A-site cation size and its nature on the fundamental ionic and electronic transport parameters. However, we believe that some more investigation is required to fully understand the ions transport character in these Bi-halide SCs. The rate of ion migration is not clear yet if it is slow and fast in comparison to other analogs. We used the temperature-dependent measurement to investigate the ionic activation energy and focused on the single dominant process. However, depth analysis and more advanced experiments are required to understand the nonlinear process and multiple transport phenomena. Addressing these issues will be helpful to understand ionic transport in more depth.

IV. CONCLUSION

In conclusion, we investigated the influence of A-cation size and its nature on the ionic and electrical properties in lead-free $A_3Bi_2I_9$SCs with the organic cation A = MA (shorter) and FA (bigger) using impedance spectroscopy with temperature variation. The introduction of a larger cation enhances the lattice constant and extends the absorbance region.
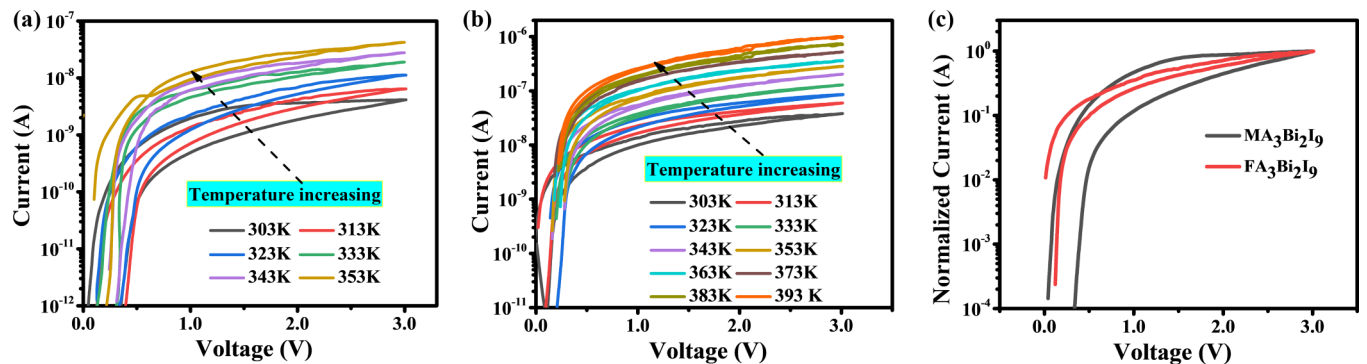

FIG. 5. Current-voltage characteristics with the temperature dependence for the (a) $MA_3Bi_2I_9$ and (b) $FA_3Bi_2I_9$SC. (c) Normalized current with applied bias voltage presenting the hysteresis in both of crystals.

Additionally, the acidic and polar nature, rotational dynamics, and H-bond strength of A cation also play a vital role to determine the ionic and electrical response. The higher activation energy of $FA_3Bi_2I_9SC$ guarantees the low noise and lower baseline drift in this crystal-based detector which would be for the detection performance enhancement. Furthermore, the larger FA cations reduce the trap density and demonstrate the lower degree of hysteresis in *I-V* curves. The less acidic and less polar nature of the FA cation also plays a vital role to determine the ionic and electrical response. This paper provides a fundamental understanding of the ionic and electrical transport in these lead-free SCs, which could be beneficial for making better performance and enhancing the overall stability of these SCs-based detector and device applications. In addition, the suggested problems in this field will help to make the field more advance.

[1] H. S. Jung and N. G. Park, Perovskite solar cells: From materials to devices, Small **11**, 10 (2015).

[2] S. Arya, P. Mahajan, R. Gupta, R. Srivastava, N. kumar Tailor, S. Satapathi, R. R. Sumathi, R. Datt, and V. Gupta, A comprehensive review on synthesis and applications of single crystal perovskite halides, Prog. Solid State Chem. **60**, 100286 (2020).

[3] S. Kadian, N. K. Tailor, N. Chaulagain, K. Shankar, S. Satapathi, and G. Manik, Effect of sulfur-doped graphene quantum dots incorporation on morphological, optical and electron transport properties of $CH_3NH_3PbBr_3$ perovskite thin films, J. Mater. Sci.: Mater. Electron. **32**, 17406 (2021).

[4] N. K. Tailor, S. P. Senanayak, M. Abdi-Jalebi, and S. Satapathi, Low-frequency carrier kinetics in triple cation perovskite solar cells probed by impedance and modulus spectroscopy, Electrochim. Acta **386**, 138430 (2021).

[5] N. K. Tailor, M. Abdi-Jalebi, V. Gupta, H. Hu, M. I. Dar, G. Li, and S. Satapathi, Recent progress in morphology optimization in perovskite solar cell, J. Mater. Chem. A **8**, 21356 (2020).

[6] S. A. Kulkarni, S. G. Mhaisalkar, N. Mathews, and P. P. Boix, Perovskite nanoparticles: Synthesis, properties, and novel applications in photovoltaics and LEDs, Small Methods **3**, 1800231 (2019).

[7] J. Xu, X. Li, J. Xiong, C. Yuan, S. Semin, T. Rasing, and X. H. Bu, Halide perovskites for nonlinear optics, Adv. Mater. **32**, 1806736 (2020).

[8] C. R. Kagan, D. B. Mitzi, and C. D. Dimitrakopoulos, Organic-inorganic hybrid materials as semiconducting channels in thin-film field-effect transistors, Science **286**, 945 (1999).

[9] X. Y. Chin, D. Cortecchia, J. Yin, A. Bruno, and C. Soci, Lead iodide perovskite light-emitting field-effect transistor, Nat. Commun. **6**, 7383 (2015).

[10] B. Murali, H. K. Kolli, J. Yin, R. Ketavath, O. M. Bakr, and O. F. Mohammed, Single crystals: The next big wave of perovskite optoelectronics, ACS Mater. Lett. **2**, 184 (2020).

[11] W. Ke and M. G. Kanatzidis, Prospects for low-toxicity lead-free perovskite solar cells, Nat. Commun. **10**, 965 (2019).

[12] N. K. Tailor, S. Kar, P. Mishra, A. These, C. Kupfer, H. Hu, M. Awais, M. Saidaminov, M. I. Dar, C. Brabec, and S. Satapathi, Advances in lead-free perovskite single crystals: Fundamentals and applications, ACS Mater. Lett. **3**, 1025 (2021).

[13] M. Kumar Chini, S. Goverapet Srinivasan, N. K. Tailor, Yukta, D. Salahub, and S. Satapathi, Lead-Free, stable mixed halide double perovskites $Cs_2AgBiBr_6$ and $Cs_2AgBiBr_{6-x}Cl_x$–A detailed theoretical and experimental study, Chem. Phys. **529**, 110547 (2020).

[14] N. K. Tailor and S. Satapathi, The impact of $Cs_3Bi_2Cl_9$ single crystal growth modality on its symmetry and morphology, J. Mater. Res. Technol. **9**, 7149 (2020).

[15] S. Satapathi and N. K. Tailor, Photosensitive dielectric and conductivity relaxation in lead-free $Cs_3Bi_2Cl_9$ perovskite single crystals, J. Phys. Chem. C **125**, 5243 (2021).

[16] N. K. Tailor and S. Satapathi, Structural disorder and spin dynamics study in millimeter-sized all-inorganic lead-free cesium bismuth halide perovskite single crystals, ACS Appl. Energy Mater. **3**, 11732 (2020).

[17] N. K. Tailor, P. Maity, and S. Satapathi, Observation of negative photoconductivity in lead-free $Cs_3Bi_2Br_9$ perovskite single crystal, ACS Photonics **8**, 2473 (2021).

[18] N. K. Tailor, P. Maity, M. I. Saidaminov, N. Pradhan, and S. Satapathi, Dark self-healing-mediated negative photoconductivity of a lead-free $Cs_3Bi_2Cl_9$ perovskite single crystal, J. Phys. Chem. Lett. **12**, 2286 (2021).

[19] Y. Yuan and J. Huang, Ion migration in organometal trihalide perovskite and its impact on photovoltaic efficiency and stability, Acc. Chem. Res. **49**, 286 (2016).

[20] C. Eames, J. M. Frost, P. R. F. Barnes, B. C. O'Regan, A. Walsh, and M. S. Islam, Ionic transport in hybrid lead iodide perovskite solar cells, Nat. Commun. **6**, 7497 (2015).

[21] F. Yang, W. Zuo, H. Liu, J. Song, H. Liu, J. Li, and S. M. Jain, Ion-migration and carrier-recombination inhibition by the cation-π interaction in planar perovskite solar cells, Org. Electron. **75**, 105387 (2019).

[22] J. S. Yun, J. Seidel, J. Kim, A. M. Soufiani, S. Huang, J. Lau, N. J. Jeon, S. Il Seok, M. A. Green, and A. Ho-Baillie, Critical role of grain boundaries for ion migration in formamidinium and methylammonium lead halide perovskite solar cells, Adv. Energy Mater. **6**, 1600330 (2016).

[23] Y. Zhao, W. Zhou, Z. Han, D. Yu, and Q. Zhao, Effects of ion migration and improvement strategies for the operational stability of perovskite solar cells, Phys. Chem. Chem. Phys. **23**, 94 (2021).

[24] M. Yanagida, Y. Shirai, D. B. Khadka, and K. Miyano, Photoinduced ion-redistribution in CH₃NH₃PbI₃ perovskite solar cells, Phys. Chem. Chem. Phys. **22**, 25118 (2020).

[25] M. H. Futscher, M. K. Gangishetty, D. N. Congreve, and B. Ehrler, Quantifying mobile ions and electronic defects in perovskite-based devices with temperature-dependent capacitance measurements: Frequency vs time domain, J. Chem. Phys. **152**, 044202 (2020).

[26] J. W. Lee, S. G. Kim, J. M. Yang, Y. Yang, and N. G. Park, Verification and mitigation of ion migration in perovskite solar cells, APL Mater. **7**, 041111 (2019).

[27] N. K. Tailor, S. Mishra, T. Sharma, A. K. De, and S. Satapathi, Cation-dependent hot carrier cooling in the lead-free bismuth halide $A_3Bi_2I_9$ (A = FA, MA and Cs) perovskite, J. Phys. Chem. C **125**, 9891 (2021).

[28] W. Li, D. Xin, S. Tie, J. Ren, S. Dong, L. Lei, X. Zheng, Y. Zhao, and W. H. Zhang, Zero-dimensional lead-free $FA_3Bi_2I_9$ single crystals for high- performance X-ray detection, J. Phys. Chem. Lett. **12**, 1778 (2021).

[29] A. Mahapatra, R. Runjhun, J. Nawrocki, J. Lewiński, A. Kalam, P. Kumar, S. Trivedi, M. M. Tavakoli, D. Prochowicz, and P. Yadav, Elucidation of the role of guanidinium incorporation in single-crystalline MAPbI₃ perovskite on ion migration and activation energy, Phys. Chem. Chem. Phys. **22**, 11467 (2020).

[30] A. M. Katzenmeyer, V. Aksyuk, and A. Centrone, Nanoscale infrared spectroscopy: Improving the spectral range of the photothermal induced resonance technique, Anal. Chem. **85**, 1972 (2013).

[31] V. Pecunia, J. Zhao, C. Kim, B. R. Tuttle, J. Mei, F. Li, Y. Peng, T. N. Huq, R. L. Z. Hoye, N. D. Kelly, S. E. Dutton, K. Xia, J. L. MacManus-Driscoll, and H. Sirringhaus, Assessing the impact of defects on lead-free perovskite-inspired photovoltaics via photoinduced current transient spectroscopy, Adv. Energy Mater. **11**, 2003968 (2021).

[32] R. García-Rodríguez, D. Ferdani, S. Pering, P. J. Baker, and P. J. Cameron, Influence of bromide content on iodide migration in inverted $MAPb(I_{1-X}Br_x)_3$ perovskite solar cells, J. Mater. Chem. A **7**, 22604 (2019).

[33] M. H. Futscher, J. M. Lee, L. McGovern, L. A. Muscarella, T. Wang, M. I. Haider, A. Fakharuddin, L. Schmidt-Mende, and B. Ehrler, Quantification of ion migration in CH₃NH₃PbI₃ perovskite solar cells by transient capacitance measurements, Mater. Horizons **6**, 1497 (2019).

[34] Z. Kang, H. Si, M. Shi, C. Xu, W. Fan, S. Ma, A. Kausar, Q. Liao, Z. Zhang, and Y. Zhang, Kelvin probe force microscopy for perovskite solar cells, Sci. China Mater. **62**, 776 (2019).

[35] Y. Almadori, D. Moerman, J. L. Martinez, P. Leclère, and B. Grévin, Multimodal noncontact atomic force microscopy and kelvin probe force microscopy investigations of organolead tribromide perovskite single crystals, Beilstein J. Nanotechnol. **9**, 1695 (2018).

[36] D. W. Ferdani, S. R. Pering, D. Ghosh, P. Kubiak, A. B. Walker, S. E. Lewis, A. L. Johnson, P. J. Baker, M. S. Islam, and P. J. Cameron, Partial cation substitution reduces iodide ion transport in lead iodide perovskite solar cells, Energy Environ. Sci. **12**, 2264 (2019).

[37] W. Gao, C. Chen, C. Ran, H. Zheng, H. Dong, Y. Xia, Y. Chen, and W. Huang, A-site cation engineering of metal halide perovskites: Version 3.0 of efficient tin-based lead-free perovskite solar cells, Adv. Funct. Mater. **30**, 2000794 (2020).

[38] R. Kumar, P. Srivastava, and M. Bag, Role of A-site cation and x-site halide interactions in mixed-cation mixed-halide perovskites for determining anomalously high ideality factor and the super-linear power law in Ac ionic conductivity at operating temperature, ACS Appl. Electron. Mater. **2**, 4087 (2020).

[39] X. Zhao, J. Dong, D. Wu, J. Zhou, J. Feng, Y. Yao, C. Y. Xu, S. Zheng, X. Tang, and Q. Song, Impact of A-site cations on fluorescence quenching in organic-inorganic hybrid perovskite materials, J. Phys. Chem. C **125**, 11524 (2021).

[40] P. Srivastava, R. Kumar, and M. Bag, Discerning the role of an A-site cation and x-site anion for ion conductivity tuning in hybrid perovskites by photoelectrochemical impedance spectroscopy, J. Phys. Chem. C **125**, 211 (2021).

[41] M. Faizan, K. C. Bhamu, S. H. Khan, G. Murtaza, and X. He, Computational study of defect variant perovskites A2BX6 for photovoltaic applications, arXiv:2002.07543.

[42] J. He, W. H. Fang, and R. Long, Unravelling the effects of A-site cations on nonradiative electron-hole recombination in lead bromide perovskites: Time-domain *ab initio* analysis, J. Phys. Chem. Lett. **9**, 4834 (2018).

[43] H. Ryu, H. R. Byun, K. M. Mccall, D. Y. Park, T. J. Kim, M. S. Jeong, M. G. Kanatzidis, and J. I. Jang, Role of the A - site cation in low-temperature optical behaviors of $APbBr_3$ (A = Cs, CH₃NH₃), J. Am. Chem. Soc. **143**, 2340 (2021).

[44] Y. Liu, B. G. Sumpter, J. K. Keum, B. Hu, M. Ahmadi, and O. S. Ovchinnikova, Strain in metal halide perovskites: The critical role of A-site cation, ACS Appl. Energy Mater. **4**, 2068 (2021).

[45] See Supplemental Material at http://link.aps.org/supplemental/10.1103/PhysRevMaterials.6.045401 for an optical image of crystal, xrd of precursors, calculated bandgap using tauc plot, Raman spectra, impedance results, temperature-dependent conductivity, as well as dark current density.

[46] G. Fisicaro, A. La Magna, A. Alberti, E. Smecca, G. Mannino, and I. Deretzis, Local order and rotational dynamics in mixed a - cation lead iodide perovskites, J. Phys. Chem. Lett. **11**, 1068 (2020).

[47] A. Amat, E. Mosconi, E. Ronca, C. Quarti, P. Umari, M. K. Nazeeruddin, M. Grätzel, and F. De Angelis, Cation-induced band-gap tuning in organohalide perovskites: Interplay of spin-orbit coupling and octahedra tilting, Nano Lett. **14**, 3608 (2014).

[48] D. Ghosh, A. R. Smith, A. B. Walker, and M. S. Islam, Mixed a - cation perovskites for solar cells: Atomic-scale insights into structural distortion, hydrogen bonding, and electronic properties, Chem. Mater. **30**, 5194 (2018).

[49] X. Huang, S. Huang, P. Biswas, and R. Mishra, Band gap insensitivity to large chemical pressures in ternary bismuth iodides for photovoltaic applications, J. Phys. Chem. C **120**, 28924 (2016).

[50] T. Shi, H. S. Zhang, W. Meng, Q. Teng, M. Liu, X. Yang, Y. Yan, H. L. Yip, and Y. J. Zhao, Effects of organic cations on the defect physics of tin halide perovskites, J. Mater. Chem. A **5**, 15124 (2017).

[51] C. Wu, D. Guo, P. Li, S. Wang, A. Liu, and F. Wu, A study on the effects of mixed organic cations on the structure and properties in lead halide perovskites, Phys. Chem. Chem. Phys. **22**, 3105 (2020).

[52] Y. Lin, Y. Bai, Y. Fang, Q. Wang, Y. Deng, and J. Huang, Suppressed ion migration in low-dimensional perovskites, ACS Energy Lett. **2**, 1571 (2017).

[53] R. Zhuang, X. Wang, W. Ma, Y. Wu, X. Chen, L. Tang, H. Zhu, J. Liu, L. Wu, W. Zhou, X. Liu, and Y. (Michael) Yang, Highly sensitive x-ray detector made of layered perovskite-like $(NH_4)_3Bi_2I_9$ single crystal with anisotropic response, Nat. Photonics **13**, 602 (2019).

[54] E. Mosconi and F. De Angelis, Mobile ions in organohalide perovskites: Interplay of electronic stucture and dynamics, ACS Energy Lett. **1**, 182 (2016).

[55] A. Mahapatra, N. Parikh, H. Kumari, M. K. Pandey, M. Kumar, D. Prochowicz, A. Kalam, M. M. Tavakoli, and P. Yadav, Reducing ion migration in methylammonium lead tri-bromide single crystal via lead sulfate passivation, J. Appl. Phys. **127**, 185501 (2020).

[56] X. Zheng, W. Zhao, P. Wang, H. Tan, M. I. Saidaminov, S. Tie, L. Chen, Y. Peng, J. Long, and W. H. Zhang, Ultrasensitive and stable x-ray detection using zero-dimensional lead-free perovskites, J. Energy Chem. **49**, 299 (2020).

[57] G. González, Quantum theory of space charge limited current in solids, J. Appl. Phys. **117**, 084306 (2015).

[58] L. K. Ang, W. S. Koh, Y. Y. Lau, and T. J. T. Kwan, Space-charge-limited flows in the quantum regime, Phys. Plasmas **13**, 056701 (2006).

[59] X. G. Zhang and S. T. Pantelides, Theory of Space Charge Limited Currents, Phys. Rev. Lett. **108**, 266602 (2012).

[60] A. Kalam, R. Runjhun, A. Mahapatra, M. M. Tavakoli, S. Trivedi, H. Tavakoli Dastjerdi, P. Kumar, J. Lewiński, M. Pandey, D. Prochowicz, and P. Yadav, Interpretation of resistance, capacitance, defect density, and activation energy levels in single-crystalline $MAPbI_3$, J. Phys. Chem. C **124**, 3496 (2020).

[61] Y. Liu, Z. Xu, Z. Yang, Y. Zhang, J. Cui, Y. He, H. Ye, K. Zhao, H. Sun, R. Lu, M. Liu, M. G. Kanatzidis, and S. (Frank) Liu, Inch-size 0D-structured lead-free perovskite single crystals for highly sensitive stable x-ray imaging, Matter **3**, 180 (2020).